Atomic design and fine-tuning of sub-nanometric Pt catalysts to tame hydrogen generation

Jie Yang
State Key Laboratory of Coal Conversion, Institute of Coal Chemistry, Chinese Academy of Sciences; Center of Materials Science and Optoelectronics Engineering, University of Chinese Academy of Scien

Wenzhao Fu
State Key Laboratory of Chemical Engineering, East China University of Science and Technology

Chaoqiu Chen
State Key Laboratory of Coal Conversion, Institute of Coal Chemistry, Chinese Academy of Sciences

Wenyao Chen
East China University of Science and Technology

Wugen Huang
State Key Laboratory of Catalysis, Dalian Institute of Chemical Physics, Chinese Academy of Sciences, Dalian 116023, China. https://orcid.org/0000-0003-4270-5044

Ruoou Yang
Shanghai Synchrotron Radiation Facility, Zhangjiang National Lab, Shanghai Advanced Research Institute, Chinese Academy of Sciences

Qing-Qiang Kong
Institute of Coal Chemistry, Chinese Academy of Sciences

Baiyan Zhang
State Key Laboratory of Coal Conversion, Institute of Coal Chemistry, Chinese Academy of Sciences

Jixiao Zhao
State Key Laboratory of Coal Conversion, Institute of Coal Chemistry, Chinese Academy of Sciences; Center of Materials Science and Optoelectronics Engineering, University of Chi

Cheng-Meng Chen
Institute of Coal Chemistry, Chinese Academy of Sciences https://orcid.org/0000-0003-4259-9923

Jun Luo
School of Materials Science and Engineering, Tianjin University of Technology https://orcid.org/0000-0001-5084-2087

Fan Yang
Dalian Institute of Chemical Physics https://orcid.org/0000-0002-1406-9717

Xuezhi Duan
East China University of Science and Technology

Zheng Jiang
Shanghai Advanced Research Institute https://orcid.org/0000-0003-4297-464X

Yong Qin (qinyong@sxicc.ac.cn)
Institute of Coal Chemistry, Chinese Academy of Sciences https://orcid.org/0000-0002-5567-1464

Article

Keywords: sub-nanometric Pt catalysts, hydrogen generation, atomic design

Posted Date: October 6th, 2020

DOI: https://doi.org/10.21203/rs.3.rs-84814/v1

Abstract

Rational synthesis of sub-nanocatalysts with controllable electronic and atomic structures remains a challenge to break the limits of traditional catalysts for superior performance. Here we report the atomic-level precise synthesis of Pt/graphene sub-nanocatalysts (from single atom, dimer, and to cluster) by atomic layer deposition, achieved by a novel high temperature pulsed ozone strategy to controllably pre-create abundant in-plane epoxy groups on graphene as anchoring sites. The specific in-plane epoxy structure endows the deposited Pt species with outstanding uniformity, controllability and stability. Their size-depended electronic and geometric effects have been observed for ammonia borane hydrolysis, revealing a volcano-type dependence of intrinsic activity on their sizes. Their active site structures have been identified based on extensive characterizations, dynamic compensation effect, kinetic isotope experiments and density function theory simulation. The Pt dimers show the highest catalytic activity and good durability than Pt single atoms and nanoparticles, ascribed to the unique C-Pt-Pt-O (C5Pt2O, metal-metal bond dimer) active site structure. Our work provides new insights into the precise tailoring and catalytic mechanism in sub-nanometer level.

Introduction

Downsizing metal nanocatalysts to the sub-nanometric ones (cluster and single atom) has been a powerful yet challenging strategy to break the limits of traditional catalysts for superior catalytic performance in addition to ultra-high atom utilization.[1–7] For such unique complex sub-nanostructure bonding with the support, a change of even only one atom usually brings significant electronic and geometric properties compared to traditional nanocatalysts.[6–11] This calls for more fundamental understanding, because classical catalytic theories are not entirely applicable to sub-nanocatalysis. For example, some researches have revealed that single-atom catalysis breaks limitations of Brønsted-Evans-Polanyi (BEP) relation and kinetic compensation effects in some certain reactions.[12–15] Despite great progress achievements, it remains a most challenging task to rationally fabricate controllable electronic and atomic structures of sub-nanocatalysts, especially for cluster catalysts, which are basically based on the atomic geometric arrangement and changeable ligands.[16] Currently, the clusters with a few atoms are mainly prepared by mass selection/soft landing and ligand-protected method.[17–20] The former is limited to deposit onto a film surface under ultra-high vacuum conditions. The later often suffers from certain metal poison by the strong ligands. Therefore, it is critically important to develop new strategies to precisely design sub-nanocatalysts from single atom to cluster with both certain atom numbers and unique complex structure by understanding the underlying nature of their structure-property relations.

Atomic layer deposition (ALD) is considered to be an ideal method to accurately construct metal sub-nanocatalysts with tunable atom numbers due to its self-limiting, atom-by-atom growth and the ample scope of materials that can be deposited.[21–24] However, the successful examples for preparing sub-nanocatalysts with controllable atom numbers through ALD (single atom and cluster) is still very limited, mainly due to the strong tendency of migration and aggregation of metal species during the ALD process.

Yan et al. prepared Co single atom catalysts with controllable loading by tuning Co ALD cycle number and using the out-of-plane epoxy group, regenerated in situ by ozone (O_3) etching during ALD process, as anchoring sites for Co atoms in the following cycle.[25] But it is still unclear whether this strategy is valid for controllably preparing metal cluster catalysts, especially for noble metals such as Pt. In contrast to Co, Pt itself could act as active nucleation site for ALD process,[26, 27] which competes with the in-situ generated epoxy groups for bonding with Pt precursors in the following ALD cycle, resulting in difficulties in formation of uniform Pt clusters. To avoid the interference of the in-situ generated epoxy in the construction of Pt cluster by ALD, Lu and coworkers synthesized a Pt_2 complex containing Pt-O-Pt structure on graphene with phenolic hydroxyl as anchoring sites by carefully controlling the conditions of two sequential Pt ALD cycles, in which O_2 was selected in the first cycle to prevent from creating any additional nucleation sites while lower temperature and O_3 was used in the second cycle to avoid metal aggregation.[11] The Pt_2 complex exhibited high activity and improved stability for hydrolysis of ammonia borane (AB). However, it should be noted that the Pt-O-Pt structure is essentially unstable at relative high temperature or reducing conditions due to the occurrence of deoxygenation. In addition, they also found that the Pt_1 single atoms bonded with the phenolic hydroxyl groups showed poor stability. These studies strongly suggest that besides cycle number of ALD, fine-tuning of the microstructure and population of anchoring sites on support surface, which is still a great challenge, is another prerequisite for regulating the nucleation and growth of metal in each ALD cycle, and in turn achieving high active and stable sub-nanocatalysts with controlled atom numbers and structures.

Hydrogen is recognized as an ideal energy carrier. As a remarkable structure-sensitive reaction, hydrolysis of AB to facilely generate hydrogen has emerged as a model reaction to understand the underlying nature of the metal particle size, electronic and interfacial effects.[11, 28–32] Herein, we develop a new strategy to regulate the nucleation and growth of Pt in ALD for precisely tailoring Pt/graphene sub-nanocatalysts by pre-creating extremely abundant in-plane epoxy groups with high stability as anchoring sites for Pt deposition via tunable pulsed O_3 treatment. The amount and density of the pre-created in-plane epoxy groups far exceed that generated in-situ during every ALD cycle, so the interference of the latter in the precise construction of Pt cluster during sequential ALD process could be avoid. By controlling the cycle numbers of O_3 pulse and Pt ALD, we have realized atomic-level precise synthesis of Pt/graphene sub-nanocatalysts from single atom, dimer, and to cluster catalyst. Their size-dependent electronic and geometric effects and unique active structures have been systematically investigated for AB hydrolysis. A volcano-type dependence of intrinsic activity on the size of Pt sub-nanocatalysts has been clearly demonstrated. The Pt dimers show the highest catalytic activity, 2.6 times higher than those of Pt single atoms. The sub-nanometric Pt species with in-plane epoxy groups as anchoring sites exhibit excellent stability. The excellent performance is ascribed to the unique C-Pt-Pt-O (C_5Pt_2O) active site structure (genuine dimer with Pt-Pt bond) supported by density function theory (DFT) calculations. Correlation between different Pt species and reaction activity or activation energy in AB hydrolysis has been proposed. Our work can guide the precise design of sub-nanocatalysts and active site structures and provide insights into the catalytic mechanism in sub-nanometer level.

Results And Discussion

Fabrication and superior performance of Pt/epoxy-rich graphene sub-nanocatalysts. It is well-known that the activity and stability of metal sub-nanocatalysts is highly depended on the structure and stability of anchoring sites on supports. For graphene, among various oxygen-containing functional groups (OCGs), the in-plane epoxy groups have excellent thermal stability, which exist stably even at high temperatures above 1000 K,[33] as proved by the DFT calculation results (Figure S1a and S1b). Clearly, the in-plane epoxy shows a higher binding energy than the out-of-plane epoxy, suggesting that the in-plane epoxy has a better stability. In addition, structurally, the single metal atom bonded with in-plane epoxy is closer to graphene basal plane than that bonded with out-of-plane epoxy or phenol. So it is reasonable to expect that the metal atoms introduced in the following ALD cycle would simultaneously bond with the single metal atom and graphene, achieving more stable metal cluster containing metal-metal bond and peculiar coordination environment. Accordingly, our study began by precisely engineering the thermally and chemically stable in-plane epoxy groups on graphene as the anchoring sites to enable the growth of sub-nanometric Pt species with controllable size, good stability and unique complex structure. As schematically shown in Scheme 1, a new strategy based on the pretreatment of multiple O_3 pulses is developed to predominantly yield abundant epoxy groups on graphene denoted as epoxy-rich graphene, distinguished from extensively reported acid etching method,[33–35] which yields graphene oxides with multi-kind OCGs (such as ester, phenol, carbonyl and carboxyl groups). To minimize the adverse effects of the initial OCGs on the pretreatment process, OCGs-deficient graphene prepared by thermal reduction of graphene oxide at 1600 °C,[36–38] i.e., G1600, was selected as starting material (see details in Supplementary Information). The epoxy groups were then selectively introduced on the G1600 by multiple O_3 pulses pretreatments with the pulse, exposure, and purge times of 2, 30 and 60 s, respectively. Their contents were precisely tailored by adjusting the cycle number (y) of O_3 pulses designated as G1600-O_3-y, as confirmed by X-ray photoemission spectroscopy (XPS) and Raman measurements (Fig. 1a and Figure S1, S2 and S3), providing ideal platforms to construct Pt sub-nanocatalysts with tunable density of isolated Pt species.

Using the well-controlled epoxy-rich graphene as the substrate, we then sought to precisely synthesize Pt sub-nanocatalysts from single atom to cluster by tuning the cycle number (x) of Pt ALD (Scheme 1), denoted as xPt/G1600-O_3-y. It is obviously seen that based on inductively coupled plasma atomic emission spectrometer (ICP-AES) measurements, the Pt loadings of xPt/G1600-O_3-y (y = 30, 60, 90 and 120) are much higher than those of xPt/G1600 prepared with the same cycle number of Pt ALD (x = 1, 2, 5 and 8) (Table S1). Interestingly, the Pt loading and the content of epoxy group are observed to follow similar trends with respect to the cycle number of O_3 pulse (Fig. 1a), indicating a linear relation of the Pt loading with the content of epoxy group. Meanwhile, at a certain O_3 cycle number (i.e., y = 60), the Pt loading of xPt/G1600-O_3-y increases quite linearly with the cycle number of Pt ALD (Fig. 1a). In contrast, the Pt loading of xPt/G1600 is observed to increase non-linearly with the Pt ALD cycle number owing to the unselective deposition of Pt species over the G1600 support (Table S1 and the following HAADF-STEM and XAS measurements). These results demonstrate that the pretreatment process with the

controllable O_3 pulses is of crucial significance to create predominantly abundant epoxy groups for guaranteeing the precise fabrication of Pt/graphene sub-nanocatalysts by the ALD technique.

The as-prepared Pt/graphene sub-nanocatalysts were further evaluated for AB hydrolysis to explore their unique catalytic behaviors. As clearly shown in Figure S4, the 1Pt/G1600 catalyst prepared without the O_3 pulse pretreatment is almost inactive, while the 1Pt/G1600-O_3-y (y = 0, 30, 60, 90, 120) catalysts with the O_3 pulse pretreatment show significantly enhanced hydrogen generation rate, strongly indicating positive effects of the O_3 pulse pretreatment. Especially, the 1Pt/G1600-O_3-60 catalyst achieves the highest hydrogen generation rate among these five catalysts. More interestingly, as the Pt ALD cycle number increases, the resultant sub-nanometric xPt/G1600-O_3-60 catalysts give rise to remarkably increased hydrogen generation rate followed by a decline (Fig. 1b). Considering that increasing the Pt ALD cycle number leads to the increase in the Pt loading, a fair comparison was made to normalize the hydrogen generation activity based on the Pt loadings. All the ALD-Pt/graphene sub-nanocatalysts are found to show linear hydrogen evolution curves in the initial reaction periods, suggesting pseudo-zero order kinetics for the reaction, and thus the turnover frequency (TOF) would be easily calculated according to our previous method.[39–41]

Figure 1a summarizes the TOF values of xPt/G1600-O_3-60 catalysts. Clearly, the TOF almost double increases as the cycle number increases from one to two, followed by a steady increase until the cycle number up to 5 (5Pt/G1600-O_3-60) and then a decline with the further increase in the cycle number. In other words, the xPt/G1600-O_3-60 catalysts display a volcano-shape curve with respect to the Pt ALD cycle number, which is remarkably different from the linear relation of their Pt loadings with the Pt ALD cycle number mentioned above. This implies that these xPt/G1600-O_3-60 catalysts exhibit different geometric and/or electronic structures of catalyst active sites, which will be shown below. Meanwhile, the most active 5Pt/G1600-O_3-60 catalyst exhibits the TOF of 37134 h^{-1}, which is approximately 2.6 times that of 1Pt/G1600-O_3-60 catalyst, and such catalyst also possesses much higher durability than the Pt/C nanoparticles (NPs) catalyst. Specifically, at the sixth recycling run, the 5Pt/G1600-O_3-60 catalyst maintains 88% of the hydrogen generation rate at the first run, while the Pt/C NPs with only 29% of the hydrogen generation rate (Fig. 1c and Figure S5).[30] In addition, the durability of this catalyst is better than that of 1Pt/G1600-O_3-60 catalyst. These strongly indicate that downsizing Pt nanocatalysts to appropriate sub-nanometric ones is a promising strategy for delivering simultaneously high hydrogen generation activity and catalyst durability. Notably, at the sub-nanometric scale, all the Pt atoms almost locate at the surfaces, which are all accessible to the reactants. Therefore, this TOF is contributed by the intrinsic activity of the Pt species, calling for more fundamental understanding of sub-nanometric active Pt species and active site structures from the viewpoint of catalyst active sites.

In addition, the graphene control sample with higher contents of OCGs and phenols as dominant OCGs (Figure S6a) was also prepared by traditional Hummers method and vacuum-promoted exfoliation of graphene oxide at 600 °C (denoted as G600) and used for Pt deposition. As shown in Figure S6b and 6c,

the xPt/G600 exhibit much lower catalytic activity than that of xPt/G1600-O_3-60. Moreover, the durability of these catalysts (1Pt/G600 and 5Pt/G600, Figure S6d) is much worse than that of 5Pt/G1600-O_3-60 catalyst. Specifically, at the sixth recycling run, the 1Pt/G600 and 5Pt/G600 catalysts show only 20% and 11% of the initial hydrogen generation rate, respectively (Figure S6d). These results strongly indicate that epoxy groups play a key role on the catalytic activity and durability of Pt sub-nanocatalysts.

Unique structural and kinetics insights into Pt/epoxy-rich graphene sub-nanocatalysts. To obtain unique atomic, electronic and kinetics insights into the highly active and durable 5Pt/G1600-O_3-60 sub-nanocatalyst, we resort to advanced microscopic, spectroscopic and synchrotron radiation techniques together with kinetics analysis. Aberration-corrected high-angle annular dark-field scanning transmission electron microscopy (AC-HAADF-STEM) measurements were first carried out, and the results are shown in Fig. 2. Clearly, over the well-designed epoxy-rich G1600-O_3-60 support, the one Pt ALD cycle yields uniform Pt single atoms (Fig. 2c), whose loading is 1.1 wt%, while increasing the Pt ALD cycle number to two gives rise to the formation of Pt dimers (Fig. 2d). In contrast, over the G-1600 support without O_3 pretreatment, the one Pt ALD cycle yields the Pt single atoms of low loading of 0.1 wt% (Fig. 2a), while such single atomic Pt is easily grown to Pt clusters (~ 1 nm) in the second Pt ALD cycle (Fig. 2b). More interestingly, increasing the Pt ALD cycle number from 2 to up to 5 is observed to still facilitate the formation of Pt dimers (Fig. 2d-g,) as confirmed by the observed Pt-Pt bond lengths of 2.60 ± 0.05 Å (Figure S7), which are smaller than the Pt-Pt bond length of 2.80 Å in bulk Pt.[42, 43] However, further increasing the Pt ALD cycle leads to the appearance of Pt clusters (Fig. 2h). These results demonstrate that employing the created abundant epoxy groups on the G1600-O_3-60 as the nucleation sites of Pt ALD is a simple yet effective strategy for the precise fabrication of Pt/graphene sub-nanocatalysts at the atomic level from Pt single atoms, dimers to clusters by tailoring the Pt ALD cycle numbers.

The X-ray absorption near-edge spectroscopy (XANES) and X-ray photoelectron spectroscopy (XPS) measurements were further conducted to reveal the unique electronic structure of Pt sub-nanocatalysts. Figure 3a shows the Pt L_3-edge XANES profiles of xPt/G1600-O_3-60, 2Pt/G1600, and the reference samples Pt foil and PtO_2. The white line intensities of xPt/G1600-O_3-60 were all higher than that of Pt foil, indicating that the Pt species are partially positively charged ($Pt^{\delta+}$, $0 < \delta < 4$).[44, 45] In contrast, the white-line intensity of 2Pt/G1600 is clearly lower than those of Pt sub-nanocatalysts, suggesting lower oxidation state of Pt determined by its nanometric size (Fig. 2b). More interestingly, in the sub-nanometric size regime, the white-line intensities fluctuate (inset of Fig. 3a), i.e., the white line intensity first decreases when the Pt ALD cycle number increases from 1 to 4, followed by an abnormal increase in 5Pt/G1600-O_3-60 and then a decline in 6Pt/G1600-O_3-60. In line with this phenomenon, a size-dependent oscillation in binding energy for Pt sub-nanocatalysts was also found by XPS analysis (Fig. 3b and Table S2),[46, 47] which is probably a result of the combination of various effects such as size effect and charge transfer between Pt and graphene support. These results further reliably confirm the precise tailoring of the sub-nanometric Pt/graphene catalysts and their size-depended electronic and geometric properties. In addition, The AC-HAADF-STEM, XAFS and XPS results for the used 5Pt/G1600-O_3-60 (Figure S8) showed

that the Pt dimer structure is stable and not prone to migrate and agglomerate to nanocluster or nanoparticles under reaction conditions, consistent with above catalytic results.

Further kinetics analysis of xPt/G1600-O_3-60 (x = 1–8) sub-nanocatalysts with the unique atomic and electronic structures identified above was performed to obtain mechanistic insights into the Pt single atoms-, dimers- against clusters-catalyzed AB hydrolysis to generate hydrogen. As obviously shown in Figure S9, these catalysts retain zero-order reaction kinetics, and thus the corresponding reaction rate constants are yielded based on the slope of the linear part for each curve. Further combining with the Arrhenius equation, the activation energy (E_a) and the logarithm of pre-exponential factor (lnA) values were obtained and shown in Table S3. Among all these catalysts, the 5Pt/G1600-O_3-60 catalyst demonstrates the lowest E_a and lnA, while the highest values for the 1Pt/G1600-O_3-60 catalyst. Based on the transition state theory, the E_a and lnA represent the indications of activation and adsorption of reactants, respectively. Hence, the 5Pt/G1600-O_3-60 with the lowest lnA corresponds to the strongest interaction with the reactants in terms of their adsorption, which would facilitate the bond cleavage of reactants in terms of their activation, thus paving an explanation of its highest catalytic activity. Interestingly, the results of kinetics parameters E_a versus lnA of these catalysts demonstrate a remarkable compensation effect as shown in Fig. 3c.[48, 49] This can be further divided into three kinetics regimes: the single atom, dimer and cluster catalysts locate in the regimes of high, low and medium E_a and lnA values, respectively. In light of the previous DFT study,[50] this could be interpreted as the change in the binding energy of reaction species, which induces a switch in the kinetic regime. To be more specifically, the adsorption of AB and H_2O could be weak for the single atom catalyst, in which the catalyst surfaces are mainly covered by reaction products. With the increase of Pt size, the AB hydrolysis slowly switches from the product coverage-limited regime to the reactant activation regime. However, further increasing the Pt size would switch back to the product coverage-limited regime, due to the decreased adsorption strengthen of reactants (Fig. 3d).

Identification of sub-nanometric Pt active sites and kinetics analysis. The above-mentioned size-depended electronic and geometric properties of sub-nanometric Pt catalyst augur the specific active site structures of Pt species in xPt/G1600-O_3-60. To clarify the atomic coordination and structural signature of Pt active site, the extended X-ray absorption fine structure (EXAFS) measurements were carried out. As shown in Fig. 4a, all the xPt/G1600-O_3-60 samples show a major scattering peak at ~ 1.65 Å (without phase shift) from the Pt-O/C contributions and a very weak peak at ~ 2.42 Å from either the satellite peak of Pt-O/C or the Pt-Pt contribution, which need be further identified through the EXAFS curve fitting. In contrast, the peak at ~ 2.70 Å (without phase shift) for 2Pt/G1600 is similar to that of Pt foil and corresponds to Pt-Pt bonds, indicating that it is mainly composed of Pt clusters or Pt nanoparticles. According to the EXAFS curve fitting results of 1Pt/G1600-O_3-60 (Fig. 4a and Table S4), Pt-O/C coordination peak (average coordination number of 4.5 at a distance of 2.00 Å) is the dominant one, while the Pt-Pt contribution is significant weak with an average coordination number of only 0.5, implying that the Pt species mainly exist in the form of single atom in 1Pt/G1600-O_3-60. For xPt/G1600-O_3-60 (x =

2–5), besides the Pt-O/C coordination, a Pt-Pt contribution at a distance of ~ 2.62 Å with an average coordination number between 1.1 and 1.7 is also observed, indicating Pt dimer are predominantly formed and their contents gradually increases with the increase of Pt ALD cycles. However, for 6Pt/G1600-O_3-60, a longer Pt-Pt bond length of 2.72 Å and larger average coordination number of 2.0 are observed, indicating that a large number of Pt clusters exist in 6Pt/G1600-O_3-60. Furthermore, the wavelet transforms (WT) of Pt L-edge EXAFS also well demonstrate the different forms of Pt species in xPt/G1600-O_3-60 (x = 1–5). As shown in Fig. 4b-f, as the cycle number of Pt ALD increases, the peak of Pt-Pt bond near 2.4 Å (without phase shift) gradually moves to the high-k portion in k-space, indicating that the bonding forms of the Pt atoms change from single atom to dimer in xPt/G1600-O_3-60 (x = 1–5).

From the above-mentioned results, we can know that the specific active site structures of Pt species can be produced using the abundant epoxy groups as the anchoring sites for Pt ALD with the controllable cycle numbers. Based on the XPS and XAFS results, density function theory (DFT) calculations were conducted to determine the optimal structure of Pt single atom, dimer and cluster catalysts (Figure S10). The simulated coordination structure of the Pt single atom and dimer are C_2PtO and C_5Pt_2O (Fig. 4g and Figure S10a, b), respectively. Interesting, the Pt-Pt bond exists in Pt dimer. And the calculated bond length of Pt-Pt in Pt dimer is 2.621 Å, consistent with the XAFS result (~ 2.61 Å), but it is shorter than the Pt-Pt bond length of 2.80 Å in bulk Pt. Because the lattice of the cluster was not observed by HAADF-STEM, it is not reasonable to use Pt(111) for calculation. Moreover, the calculation time and complexity will increase exponentially for each additional Pt atom as for cluster. Therefore, Pt_4 with better stability is selected to replace cluster for DFT calculation (Figure S10c). Then the charge density of Pt atoms in all three configurations was calculated (Fig. 4g and Figure S11). It is revealed that the Pt electron loss on three configurations are − 0.1402 (Pt single atom), -0.0558 (Pt dimer) and − 0.1545 (Pt cluster). So, the Pt cluster catalyst has the most Pt electron loss, suggesting that there exist different electronic interactions between graphene and Pt species from single atom, dimer to cluster. This also explains the size-dependent oscillation in above XANES and XPS results (Fig. 3a and 3b).

Low-temperature scanning tunneling microscopy (LT-STM) was further employed to identify the atomic and electronic structure of Pt active sites. For convenient characterization, xPt/HOPG (highly oriented pyrolytic graphite)-O_3-60, which were synthesized using the same method as xPt/G1600-O_3-60, were applied for LT-STM analysis (see details in Supplementary Information). Figure 4h and 4i display the typical atomic-resolution STM and 3D atomic structure images of 1Pt/HOPG-O_3-60, respectively. The small protrusion in zone 1 of Fig. 4h is attributed to the in-plane epoxy O atoms produced by O_3 pretreatment, whose neighboring C atoms also appear to be brighter than the C atoms further away. In addition, the single Pt center is resolved as a bright spot (zone 2 in Fig. 4h), whose neighboring C and O atoms also appear brighter and exhibit a higher apparent height than other C atoms (Fig. 4i), arising from the electronic interaction between Pt single atom and neighboring C and O atoms.[51, 52] This indicates that the Pt single atoms are bound with O and C atoms on the surface of epoxy-rich HOPG-O_3-60. For 5Pt/HOPG-O_3-60, Pt single atom (Zone 2), dimer (Zone 1) and cluster (Zone 3) are all observed, which is

consistent with the AC-HAADF-STEM and XAFS results of 5Pt/G1600-O_3-60 (Fig. 4j). Specially, for Pt dimer, two adjacent bright dots were observed, being attributed to the Pt dimer (Fig. 4k). Note that the neighboring O and C atoms of one Pt atom (Atom 1 in Fig. 4k) appear brighter and exhibit a higher apparent height than those next to another Pt atom (Atom 2 in Fig. 4k), suggesting that the two Pt atoms of Pt dimer have different electronic interaction with neighboring atoms. These results are consistent with the above DFT results (Fig. 4g).

Based on the identified structures of the sub-nanometric Pt active sites, we further carried out DFT calculations to explore their impacts on the activation of water, which has been suggested involved in the rate-determining step for this reaction. The optimized most stable adsorption configurations of water molecule on the Pt single atom, dimer and cluster as well as the corresponding potential energy profiles are displayed in Fig. 5a and Figure S12. Obviously, the Pt dimer exhibits the highest water adsorption energy with the largest enlarged O-H bond length (-0.87 eV, 0.979 Å) compared with the Pt single atom (-0.78 eV, 0.977 Å) and cluster (-0.50 eV, 0.976 Å). As a result, the activation barrier for the water dissociation was calculated as 1.28, 1.13 and 1.40 eV for the Pt single atom, dimer and cluster, respectively. Hence, from the point view of theoretical calculations, the Pt dimer exhibits the lowest activation barrier for the water dissociation. To verify this, kinetic isotope experiments by replacing H_2O with D_2O as the reactant were conducted to probe the kinetic isotope effect as an indication of the capacity of water dissociation, and the results are shown in Fig. 5b and Figure S13. Obviously, the kinetic isotope effect (KIE) value follows the trend of Pt dimer < Pt cluster < Pt single atom, which is quite consistent with the DFT calculations.

The adsorptions of AB on Pt single atom, dimer and cluster catalysts were comparatively studied by DFT calculations. The optimized most stable adsorption configurations of the involved species on Pt single atom, dimer and cluster are listed in Figure S14. It can be obviously observed that AB does not dissociative adsorb on the Pt single atom, and AB dissociative adsorbs on the Pt dimer and cluster. Moreover, from the bond length of the B-H bond, the B-H bond of AB adsorbed on the Pt dimer is elongated (1.338 Å, the B-H bond length of AB is 1.218 Å). Hence, a combination of theoretical and experimental study suggests the Pt dimer, especially the 5Pt/G1600-O_3-60, demonstrates the highest capacity for the water dissociation and activation of AB, paving an explanation for its highest catalytic activity. Moreover, based on the above results, we have proposed the correlation between the Pt species (single atom, dimer, and cluster) and TOF or activation energy (E_a) for the AB hydrolysis as shown in Fig. 5c. The TOF and activation energy exhibit a volcanic relationship with the cycle number of Pt ALD, in which the higher content of Pt dimer within the catalyst gives rise to the higher reaction activity owing to the appropriate Pt electronic properties.

Conclusion

In conclusion, we have successfully developed a general method based on ALD for the controllable synthesis of single atom, dimer, and cluster catalysts. By changing the number of O_3 pre-etching cycle to

adjust the type and content of OCGs on the graphene surface, we have achieved the atomic-scale precise control from Pt single atom to cluster. The 5Pt/G1600-O_3-60 catalyst shows extremely high catalytic activity in the AB hydrolysis reaction. Kinetic experiments reveal that the 5Pt/G1600-O_3-60 catalyst has the lowest activation energy. Using G1600-O_3-60 as support, with the increase of Pt ALD cycle, the deposited Pt changes from single atom to cluster, and 5Pt/G1600-O_3-60 catalyst has the highest content of dimer. Their active site structures have been identified based on extensive characterizations, dynamic compensation effect, kinetic isotope experiments and density function theory simulation. The Pt dimers show the highest catalytic activity and good durability than Pt single atoms and nanoparticles, ascribed to the unique C-Pt-Pt-O (C_5Pt_2O, metal-metal bond dimer) active site structure. Our work can guide the precise synthesis of single atom, dimer, and cluster, and provide insights for the catalytic mechanism investigation of different active species in other catalytic reactions.

Experimental Procedures

Material. Analytical reagent grade ammonia borane complex (NH_3BH_3, AB, 97%) and PtO_2 were purchased from Sigma-Aldrich. (methylcyclopentadienyl)trimethylplatinum ($MeCpPtMe_3$, 99%) was purchased from Strem Chemicals. HOPG (0.5 cm × 0.5 cm, ZYB grade) was purchased from Bruker. Deuterium oxide (D_2O) was purchased from Sigma-Aldrich. All materials are used without further purification.

Fabrication of G1600. The G1600 (510 $m^2 \cdot g^{-1}$), provided by the Institute of Coal Chemistry, Chinese Academy of Sciences, was prepared by vacuum-promoted exfoliation of graphene oxide at 600 °C and further calcination at 1600 °C (G1600) under Ar atmosphere to remove the initial OCGs. In brief, graphene oxide (GO) was prepared firstly by a modified Hummers' method.[36] Then, the as-prepared GO was grounded into fine powder (~ 100 mesh), dried at 110 °C for 3 h. Next, it was placed into a quartz tube and heated from room temperature to 600 °C at a rate of 30 °C/min and dwelled at 600 °C for 20 s under under a high vacuum (< 2.0 Pa).[37] Finally, the exfoliated graphene sample was further heated to 1600 °C at a rate of 10 °C/min and kept at 1600 °C for 1 h under Ar atmosphere. The obtained graphene sample was denoted as G1600.[38]

Fabrication of epoxy-rich graphene (G1600-O_3-y). To prepare the epoxy-rich graphene, a pulsed O_3 etching process for G1600 was carried out at 270 °C on a hot-wall, closed-chamber ALD reactor with N_2 (99.999%) as carrier gas. The pulse, exposure, and purge times for O_3 were 2, 30, and 60 s, respectively. The prepared sample was named as G1600-O_3-y (y refers to the number of O_3 cycles).

Fabrication of sub-nanometric Pt catalysts (xPt/G1600-O_3-y). Pt ALD was carried out on the as-prepared G1600-O_3-y to fabricate sub-nanometric Pt (from single atom, dimer, to cluster) using $MeCpPtMe_3$ (Strem Chemicals, 99%) and O_3 as precursors at 270 °C in the same ALD reactor. The $MeCpPtMe_3$ was kept at 60 ˚C to provide a sufficient vapor pressure. For each ALD cycle, the pulse, exposure, and purge times for $MeCpPtMe_3$ were 0.5, 10, and 20 s and those for O_3 were 1, 10, and 20 s, respectively. Nitrogen (99.999%)

was used as the carrier and purge gas. Different cycles of Pt ALD were carried out to obtain a series of the catalysts with controlled Pt size and loading (denoted as xPt/G1600-O_3-y, x and y refer to the number of Pt ALD and pulsed O_3-etching cycles, respectively). As a control experiment, Pt ALD was also carried out on the pristine G1600 substrate for different cycles under the same ALD conditions (denoted as xPt/G1600, x is the number of Pt ALD cycles).

Fabrication of 1Pt/HOPG-O $_3$ -60 and 5Pt/HOPG-O $_3$ -60 model catalysts. Firstly, 60 cycles of pulsed O_3 etching process were also carried out on the HOPG surface to introduce epoxy groups (denoted as HOPG-O_3-60). Then, Pt ALD was carried out on the HOPG-O_3-60 under the same condition as mentioned above. The resulting sample prepared by either 1or 5 ALD cycles of Pt is denoted as 1Pt/HOPG-O_3-60, and 5Pt/HOPG-O_3-60 model catalyst, respectively.

Catalyst Characterization. The Pt loading in all samples was determined by an inductively coupled plasma atomic emission spectrometer (ICP-AES, Thermo ICAP 6300). Aberration-corrected high-angle annular dark-field scanning transmission electron microscopy (AC-HAADF-STEM) was performed on a JEOL 2100F (FEI, Titan Cubed Themis G2 300) at 200 keV. Fourier transform infrared spectra (FTIR) were collected with a Bruker Tensor 27 spectrometer. X-ray photoelectron spectra (XPS) were recorded on an ESCALab-250 X photoelectron spectrometer using an Al Kα source (1486.6 eV). The Raman spectra was taken by a high-resolution laser confocal fibre Raman spectrometer (Horiba Jobin Yvon, Palaiseau, France) at an excitation wavelength of 514 nm. For low-temperature scanning tunnelling microscopy (LT-STM) characterization, the HOPG sample was cut by a grid with ~3 mm intervals. LT-STM was performed on a Createc low-temperature STM system consisting of STM chamber with base pressure below 4×10^{-11} mbar and preparation chamber.[53] To eliminate the possible pollutants adsorbed on HOPG, the samples were heated to 500 K under UHV before LT-STM characterization. LT-STM images were taken with an electrochemically etched W tip at 78 K and processed using the SPIP software from Image Metrology. The X-ray absorption spectroscopy experiments at the Pt L_3 edge (11564 eV) were conducted on the BL14W1 beamline of the Shanghai Synchrotron Radiation Facility (SSRF) operated at 3.5 GeV under 'top-up' mode with a constant current of 210 mA. A Si (111) double-crystal monochromator was used to reduce the harmonic component of the monochrome beam. Pt foil and PtO_2 were used as reference samples and measured in transmission mode. The prepared Pt-based catalysts were measured in fluorescence mode. The energy was calibrated according to the absorption edge of a pure Pt foil. Athena and Artemis codes were used to extract the data and fit the profiles.

DFT Calculations. All the DFT calculations in this work were implemented in the Vienna AB-initio Simulation Program (VASP).[54] The interaction between the valence electrons and the core was described by the projected augmented wave (PAW) method, and the cut-off energy for the plane wave basis set was 450 eV.[55, 56] The exchange-correlation functional was GGA-PBE,[57] and the Monkhorst – Pack meshes of 2 × 2 × 2 k-point samplings in the surface Brillouin zones were used for the surfaces.[58] For all the calculations, the geometry optimization was converged until the forces on each atom were < 0.03 eV/Å and the total energy differences were < 10^{-5} eV. The dimer method was used to determine the transition

states of the elementary steps of H_2O dissociation.[59] Moreover, the vibrational frequencies were analysed to evaluate if a transition state with only one imaginary frequency. The H_2O activation energy was calculated as $\Delta E_a = E_{TS} - E_{adsH2O}$, where the E_{TS} is the energy of the TS, the E_{adsH2O} is the adsorption energy of the H_2O. The adsorption energy was calculated by the following equation:

$$E_{ads} = E_{ads/surface} - E_{H2O} - E_{surface}$$

where $E_{ads/surface}$ is the total energy of the surface adsorbed with the species, $E_{surface}$ is the total energy of the clean surface, and E_{H2O} is the total energy of isolated H_2O. The Bader analysis was implemented with a fast algorithm, and the core charge density was included in the partitioning.[60, 61] The charge density difference images were obtained by VESTA visualization software, and calculated as $\Delta\rho(r) = \rho_{total}(r) - \rho_{Pt}(r) - \rho_{surface}(r)$, where the $\rho_{total}(r)$ is the electron density of the total surface, the $\rho_{Pt}(r)$ is the electron density of the Pt atoms and the $\rho_{surface}(r)$ is the electron density of all the other atoms.

Catalytic hydrolysis of AB. Hydrolysis of AB was carried out in a three-necked flask at 25 ± 0.5 °C under atmospheric pressure. Briefly, prior to the reaction, a certain amount of catalyst was first added to a flask containing 10 mL deionized water. Then, 1.5 mmol AB was added into the flask at a stirring rate of 700 rpm. The volume of hydrogen gas evolved during the reaction was measured by a typical water-filled gas burette.

The initial turnover frequency (TOF) (AB conversion was 10%) of the catalysts was calculated according to Eq. (1):

$$TOF = \frac{n_{H2}}{n_{Pt} \times t} \quad (1)$$

Here n_{H2} is the molar of H_2, n_{Pt} is the total molar of Pt in the samples, and t is the reaction time (h).

Catalyst durability in the hydrolysis reaction of AB. Catalyst durability in the hydrolysis reaction of AB was investigated at 25 ± 0.5 °C. Any remaining H_2 in the reaction system was removed by N_2 after the hydrolysis reaction of AB was complete. Then, another equivalent of AB (1.5 mmol) was added to the reaction system and the hydrolysis reaction of AB was conducted again. The same process was repeated six times, and the experimental data were recorded.

Kinetic experiments. The kinetic experiments were carried out for the xPt/G1600-O_3-60 (x = 1–8) catalyst at different temperatures (15–35 °C). According to our previous work[30, 62] the initial reaction rates can be described as $r = kc^n = k$ (n = 0), where k and c are the reaction rate constant and concentration of AB, respectively. k can be obtained by fitting Arrhenius curves at different temperatures, and according to the Arrhenius equation, E_a for the five catalysts was calculated.

Isotopic experiments. Isotopic experiments for xPt/G1600-O_3-60 (x = 1, 2, 5, 6, 8) were also carried out by replacing H_2O with D_2O. The KIE values of different samples were calculated from the corresponding rate constants with H_2O and D_2O as reactant respectively, i.e., KIE = k_H/k_D.

Declarations

Data availability.

All relevant data is available from the author upon reasonable request.

Author contributions

Y.Q. and C.C. conceived the idea and supervised the work. J.Y. and C.C. designed the experiments, catalyst preparation, characterization and catalytic reaction tests. W.F., W.C. and X.D. performed the theoretical calculation and the kinetic analyses. R.Y and Z.J. performed the XAS analysis. W.H. and F.Y. conducted the LT-STM measurement and analysis. Q.K. and C.-M.C. performed graphene synthesis. J.L. conducted the HAADF-STEM measurements. B.Z. and J.Z. assisted catalyst characterization and catalytic performance tests. J.Y., C.C., X.D., Z.J., and Y.Q. wrote the manuscript. All authors discussed the results and assisted during manuscript preparation.

Acknowledgements

We acknowledge the financial support from the National Natural Science Foundation of China (21872161, U1832208, 21673269), the National Science Fund for Distinguished Young Scholars (21825204), the National Key R&D Program of China (2017YFA0700101) and Beijing Key Laboratory of Ionic Liquids Clean Process. EXAFS studies were carried out at the BL14W1 beamline at the Shanghai Synchrotron Radiation Facility, Shanghai Institute of Applied Physics, Shanghai, PR China.

Declaration of interests

The authors declare no competing interests.

References

1. Wang A, Li J, Zhang T. Heterogeneous single-atom catalysis. *Nature Reviews Chemistry* **2**, 65–81 (2018).
2. Cui X, Li W, Ryabchuk P, Junge K, Beller M. Bridging homogeneous and heterogeneous catalysis by heterogeneous single-metal-site catalysts. *Nature Catalysis* **1**, 385–397 (2018).

3. Kaiser SK, *et al.* Nanostructuring unlocks high performance of platinum single-atom catalysts for stable vinyl chloride production. *Nature Catalysis* **3**, 376–385 (2020).
4. Ji S, Chen Y, Wang X, Zhang Z, Wang D, Li Y. Chemical Synthesis of Single Atomic Site Catalysts. *Chemical Reviews*, (2020).
5. DeRita L, *et al.* Structural evolution of atomically dispersed Pt catalysts dictates reactivity. *Nature Materials* **18**, 746–751 (2019).
6. Du Y, Sheng H, Astruc D, Zhu M. Atomically Precise Noble Metal Nanoclusters as Efficient Catalysts: A Bridge between Structure and Properties. *Chemical Reviews* **120**, 526–622 (2020).
7. Guo X, Gu J, Lin S, Zhang S, Chen Z, Huang S. Tackling the Activity and Selectivity Challenges of Electrocatalysts toward the Nitrogen Reduction Reaction via Atomically Dispersed Biatom Catalysts. *Journal of the American Chemical Society* **142**, 5709–5721 (2020).
8. Liu L, Corma A. Metal Catalysts for Heterogeneous Catalysis: From Single Atoms to Nanoclusters and Nanoparticles. *Chemical Reviews* **118**, 4981–5079 (2018).
9. Pan Y, Zhang C, Liu Z, Chen C, Li Y. Structural Regulation with Atomic-Level Precision: From Single-Atomic Site to Diatomic and Atomic Interface Catalysis. *Matter* **2**, 78–110 (2020).
10. Liu L, Díaz U, Arenal R, Agostini G, Concepción P, Corma A. Generation of subnanometric platinum with high stability during transformation of a 2D zeolite into 3D. *Nature Materials* **16**, 132–138 (2017).
11. Yan H, *et al.* Bottom-up precise synthesis of stable platinum dimers on graphene. *Nature Communications* **8**, 1070 (2017).
12. Sun G, *et al.* Breaking the scaling relationship via thermally stable Pt/Cu single atom alloys for catalytic dehydrogenation. *Nature Communications* **9**, 4454 (2018).
13. Pérez-Ramírez J, López N. Strategies to break linear scaling relationships. *Nature Catalysis* **2**, 971–976 (2019).
14. Darby MT, Stamatakis M, Michaelides A, Sykes ECH. Lonely Atoms with Special Gifts: Breaking Linear Scaling Relationships in Heterogeneous Catalysis with Single-Atom Alloys. *The Journal of Physical Chemistry Letters* **9**, 5636–5646 (2018).
15. Huang Z-F, Song J, Dou S, Li X, Wang J, Wang X. Strategies to Break the Scaling Relation toward Enhanced Oxygen Electrocatalysis. *Matter* **1**, 1494–1518 (2019).
16. Ding S, Hülsey MJ, Pérez-Ramírez J, Yan N. Transforming Energy with Single-Atom Catalysts. *Joule* **3**, 2897–2929 (2019).
17. Beniya A, Higashi S, Ohba N, Jinnouchi R, Hirata H, Watanabe Y. CO oxidation activity of non-reducible oxide-supported mass-selected few-atom Pt single-clusters. *Nature Communications* **11**, 1888 (2020).
18. Vajda S, White MG. Catalysis Applications of Size-Selected Cluster Deposition. *ACS Catalysis* **5**, 7152–7176 (2015).

19. Tyo EC, Vajda S. Catalysis by clusters with precise numbers of atoms. *Nature Nanotechnology* **10**, 577–588 (2015).
20. Li Z, *et al.* Well-Defined Materials for Heterogeneous Catalysis: From Nanoparticles to Isolated Single-Atom Sites. *Chemical Reviews* **120**, 623–682 (2020).
21. Zhao J-X, *et al.* Selectivity Regulation in Au-Catalyzed Nitroaromatic Hydrogenation by Anchoring Single-Site Metal Oxide Promoters. *ACS Catalysis* **10**, 2837–2844 (2020).
22. Zhang J, *et al.* Origin of synergistic effects in bicomponent cobalt oxide-platinum catalysts for selective hydrogenation reaction. *Nature Communications* **10**, 4166 (2019).
23. Gao Z, Qin Y. Design and Properties of Confined Nanocatalysts by Atomic Layer Deposition. *Accounts of Chemical Research* **50**, 2309–2316 (2017).
24. Zhang J, *et al.* Porous TiO2 Nanotubes with Spatially Separated Platinum and CoOx Cocatalysts Produced by Atomic Layer Deposition for Photocatalytic Hydrogen Production. *Angewandte Chemie International Edition* **56**, 816–820 (2017).
25. Yan H, *et al.* Atomic engineering of high-density isolated Co atoms on graphene with proximal-atom controlled reaction selectivity. *Nat Commun* **9**, 3197 (2018).
26. Singh JA, *et al.* Area-Selective Atomic Layer Deposition of Metal Oxides on Noble Metals through Catalytic Oxygen Activation. *Chemistry of Materials* **30**, 663–670 (2018).
27. Parsons GN, Clark RD. Area-Selective Deposition: Fundamentals, Applications, and Future Outlook. *Chemistry of Materials* **32**, 4920–4953 (2020).
28. Zhu Q-L, Xu Q. Liquid organic and inorganic chemical hydrides for high-capacity hydrogen storage. *Energy & Environmental Science* **8**, 478–512 (2015).
29. Chen W, *et al.* Mechanistic Insight into Size-Dependent Activity and Durability in Pt/CNT Catalyzed Hydrolytic Dehydrogenation of Ammonia Borane. *Journal of the American Chemical Society* **136**, 16736–16739 (2014).
30. Zhang J, *et al.* Synergistic effects in atomic-layer-deposited PtCox/CNTs catalysts enhancing hydrolytic dehydrogenation of ammonia borane. *Applied Catalysis B: Environmental* **235**, 256–263 (2018).
31. Chen W, *et al.* Unique reactivity in Pt/CNT catalyzed hydrolytic dehydrogenation of ammonia borane. *Chemical Communications* **50**, 2142–2144 (2014).
32. Chen W, *et al.* Polymer decoration of carbon support to boost Pt-catalyzed hydrogen generation activity and durability. *Journal of Catalysis* **385**, 289–299 (2020).
33. Bagri A, Mattevi C, Acik M, Chabal YJ, Chhowalla M, Shenoy VB. Structural evolution during the reduction of chemically derived graphene oxide. *Nat Chem* **2**, 581–587 (2010).
34. Su C, Loh KP. Carbocatalysts: Graphene Oxide and Its Derivatives. *Accounts of Chemical Research* **46**, 2275–2285 (2013).
35. Su C, *et al.* Probing the catalytic activity of porous graphene oxide and the origin of this behaviour. *Nature Communications* **3**, 1298 (2012).

36. Chen C, *et al.* Self-Assembled Free-Standing Graphite Oxide Membrane. *Advanced Materials* **21**, 3007–3011 (2009).
37. Lv W, *et al.* Low-Temperature Exfoliated Graphenes: Vacuum-Promoted Exfoliation and Electrochemical Energy Storage. *ACS Nano* **3**, 3730–3736 (2009).
38. Chen C-M, Zhang Q, Yang M-G, Huang C-H, Yang Y-G, Wang M-Z. Structural evolution during annealing of thermally reduced graphene nanosheets for application in supercapacitors. *Carbon* **50**, 3572–3584 (2012).
39. Wang C, *et al.* Hydrolysis of Ammonia-Borane over Ni/ZIF-8 Nanocatalyst: High Efficiency, Mechanism, and Controlled Hydrogen Release. *Journal of the American Chemical Society* **139**, 11610–11615 (2017).
40. Wang L, *et al.* Supported Rhodium Catalysts for Ammonia–Borane Hydrolysis: Dependence of the Catalytic Activity on the Highest Occupied State of the Single Rhodium Atoms. *Angewandte Chemie International Edition* **56**, 4712–4718 (2017).
41. Sun Q, *et al.* Zeolite-Encaged Single-Atom Rhodium Catalysts: Highly-Efficient Hydrogen Generation and Shape-Selective Tandem Hydrogenation of Nitroarenes. *Angewandte Chemie International Edition* **58**, 18570–18576 (2019).
42. Li M, *et al.* Single-atom tailoring of platinum nanocatalysts for high-performance multifunctional electrocatalysis. *Nature Catalysis* **2**, 495–503 (2019).
43. Qiao B, *et al.* Single-atom catalysis of CO oxidation using Pt1/FeOx. *Nature Chemistry* **3**, 634–641 (2011).
44. Liu J, *et al.* High performance platinum single atom electrocatalyst for oxygen reduction reaction. *Nature Communications* **8**, 15938 (2017).
45. Zhang J, *et al.* Single platinum atoms immobilized on an MXene as an efficient catalyst for the hydrogen evolution reaction. *Nature Catalysis* **1**, 985–992 (2018).
46. Kaden WE, Wu T, Kunkel WA, Anderson SL. Electronic Structure Controls Reactivity of Size-Selected Pd Clusters Adsorbed on TiO < sub > 2</sub > Surfaces. *Science* **326**, 826–829 (2009).
47. Jiang Z, *et al.* Direct XPS Evidence for Charge Transfer from a Reduced Rutile TiO2(110) Surface to Au Clusters. *The Journal of Physical Chemistry C* **111**, 12434–12439 (2007).
48. Chen T, Zhang Y, Xu W. Single-Molecule Nanocatalysis Reveals Catalytic Activation Energy of Single Nanocatalysts. *Journal of the American Chemical Society* **138**, 12414–12421 (2016).
49. Ma H, Na C. Isokinetic Temperature and Size-Controlled Activation of Ruthenium-Catalyzed Ammonia Borane Hydrolysis. *ACS Catalysis* **5**, 1726–1735 (2015).
50. Bligaard T, Honkala K, Logadottir A, Nørskov JK, Dahl S, Jacobsen CJH. On the Compensation Effect in Heterogeneous Catalysis. *The Journal of Physical Chemistry B* **107**, 9325–9331 (2003).
51. Deng D, *et al.* A single iron site confined in a graphene matrix for the catalytic oxidation of benzene at room temperature. *Science Advances* **1**, e1500462 (2015).

52. Wu H, *et al.* Highly doped and exposed Cu(i)–N active sites within graphene towards efficient oxygen reduction for zinc–air batteries. *Energy & Environmental Science* **9**, 3736–3745 (2016).
53. Liu Q, *et al.* Towards the atomic-scale characterization of isolated iron sites confined in a nitrogen-doped graphene matrix. *Applied Surface Science* **410**, 111–116 (2017).
54. Kresse G, Furthmüller J. Efficiency of ab-initio total energy calculations for metals and semiconductors using a plane-wave basis set. *Computational Materials Science* **6**, 15–50 (1996).
55. Blöchl PE. Projector augmented-wave method. *Physical Review B* **50**, 17953–17979 (1994).
56. Kresse G, Joubert D. From ultrasoft pseudopotentials to the projector augmented-wave method. *Physical Review B* **59**, 1758–1775 (1999).
57. Perdew JP, Burke K, Ernzerhof M. Generalized Gradient Approximation Made Simple. *Physical Review Letters* **77**, 3865–3868 (1996).
58. Monkhorst HJ, Pack JD. Special points for Brillouin-zone integrations. *Physical Review B* **13**, 5188–5192 (1976).
59. Henkelman G, Jónsson H. A dimer method for finding saddle points on high dimensional potential surfaces using only first derivatives. *The Journal of Chemical Physics* **111**, 7010–7022 (1999).
60. Henkelman G, Arnaldsson A, Jónsson H. A fast and robust algorithm for Bader decomposition of charge density. *Computational Materials Science* **36**, 354–360 (2006).
61. Sanville E, Kenny SD, Smith R, Henkelman G. Improved grid-based algorithm for Bader charge allocation. *Journal of Computational Chemistry* **28**, 899–908 (2007).
62. Chen W, *et al.* Mechanistic and kinetic insights into the Pt-Ru synergy during hydrogen generation from ammonia borane over PtRu/CNT nanocatalysts. *Journal of Catalysis* **356**, 186–196 (2017).

Figures

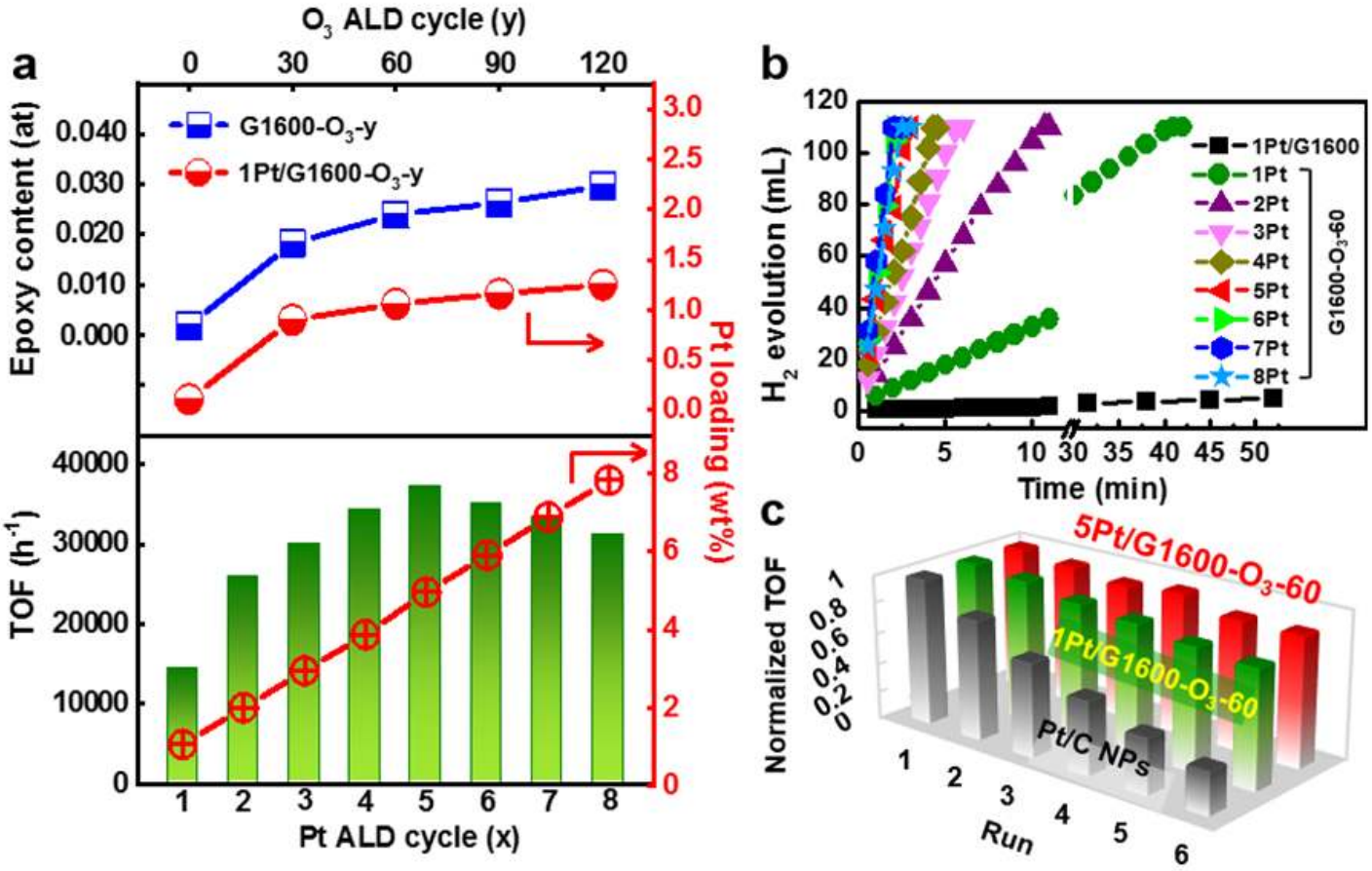

Figure 1

Superior performance of Pt/epoxy-rich graphene sub-nanocatalysts. a, The in-plane epoxy content of G1600-O3-y and Pt loading of 1Pt/G1600-O3-y catalysts as a function of the number of O3 ALD cycle (up); the Pt loading of xPt/G1600-O3-60 catalysts as a function of the number of Pt ALD cycle and the TOF values of xPt/G1600-O3-60 catalysts for AB hydrolysis (bottom). b, The hydrogen evolution as a function of reaction time over 1Pt/G1600 and xPt/G1600-O3-60 catalysts at 25 ºC. c, A comparison for the durability of 5Pt/G1600-O3-60, 1Pt/G1600-O3-60 and Pt/C NPs catalysts.

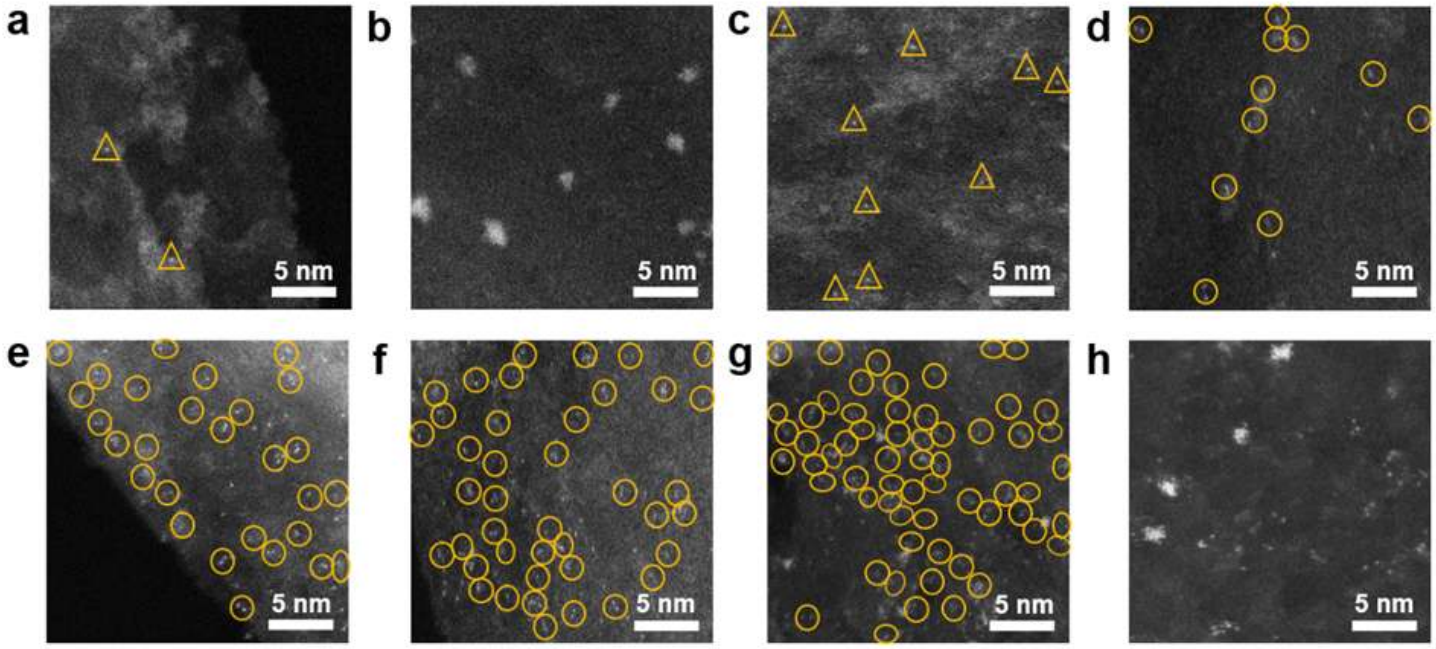

Figure 2

Atomic structures of Pt/graphene sub-nanocatalysts. a-h, AC-HAADF-STEM images of 1Pt/G1600, 2Pt/G1600, 1Pt/G1600-O3-60, 2Pt/G1600-O3-60, 3Pt/G1600-O3-60, 4Pt/G1600-O3-60, 5Pt/G1600-O3-60 and 6Pt/G1600-O3-60, respectively. Note: yellow triangles and circles refer to Pt single atom and dimer, respectively.

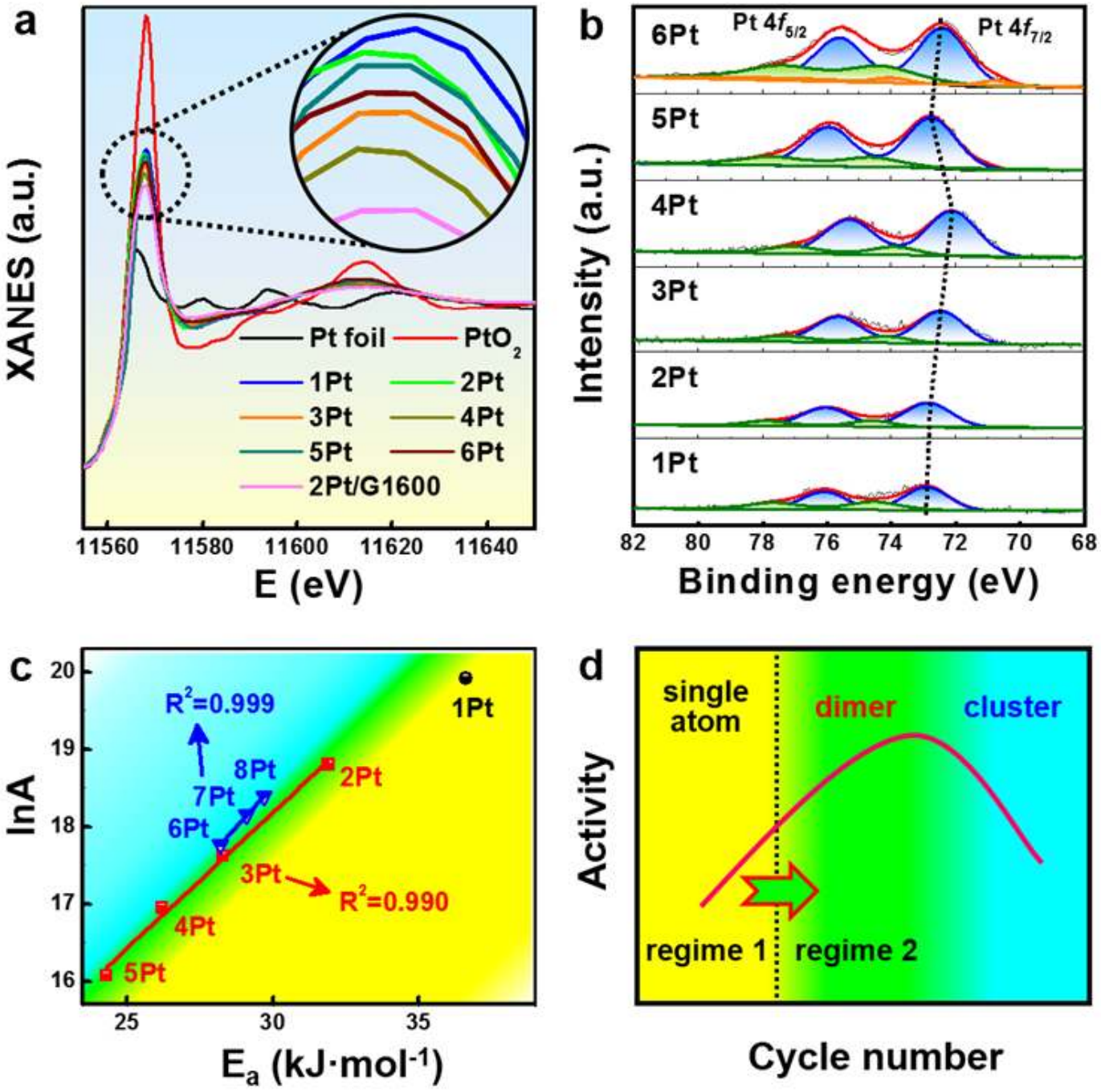

Figure 3

Unique electronic structural and kinetics insights into Pt/graphene sub-nanocatalysts. a, The Pt L3-edge XANES spectra of Pt foil, 2Pt/G1600, xPt/G1600-O3-60 (replace with xPt in the Figure 3a) and PtO2. The inserted circle area shows the corresponding white line peak. b, The high-resolution Pt 4f XPS of xPt/G1600-O3-60 (replace with xPt in the Figure 3b). c, The kinetic compensation effects of xPt/G1600-O3-60 (x=1-8, replace with xPt in the Figure 3c). The yellow, green and blue regions represent single atom, dimer and cluster, respectively. d, The schematic diagrams of reaction species, activity and kinetic regime. Among them, the yellow, green and blue regions represent single atom, dimer and cluster, respectively.

Regime 1 and regime 2 represent the product coverage-limited regime and the reactant activation regime, respectively.

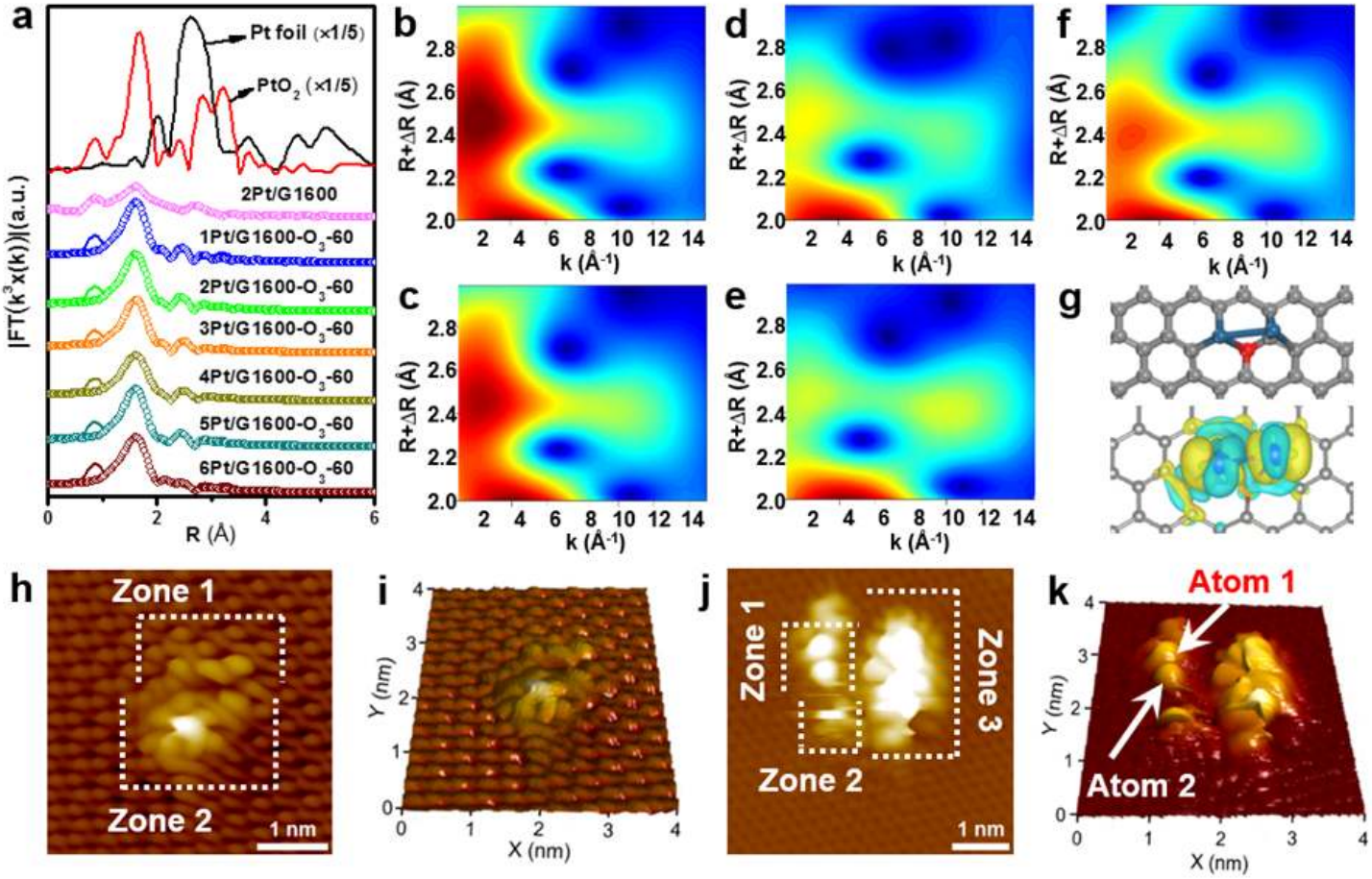

Figure 4

Identification of Pt/graphene sub-nanocatalysts. a, The EXAFS spectra and their k3-weighted fitting results of Pt foil, 2Pt/G1600, xPt/G1600-O3-60 and PtO2. b-f, Wavelet transforms for the k3-weighted EXAFS signals. From b to e are 1Pt/G1600-O3-60 to 5Pt/G1600-O3-60, respectively. g, Top view of the optimized structure and charge density difference of Pt dimer. Atom coloring: C, gray; O, red; Pt, blue. Yellow and light-blue isosurfaces represent accumulation and depletion of electronic density. h-k, Atomic resolution STM images of 1Pt/HOPG-O3-60 single atom and of 5Pt/HOPG-O3-60 dimer. Scanning parameters: h: Us=2.0 V, I=0.1 nA; j: Us=1.0 V, I=0.1 nA; i and k display the 3D atomic structures.

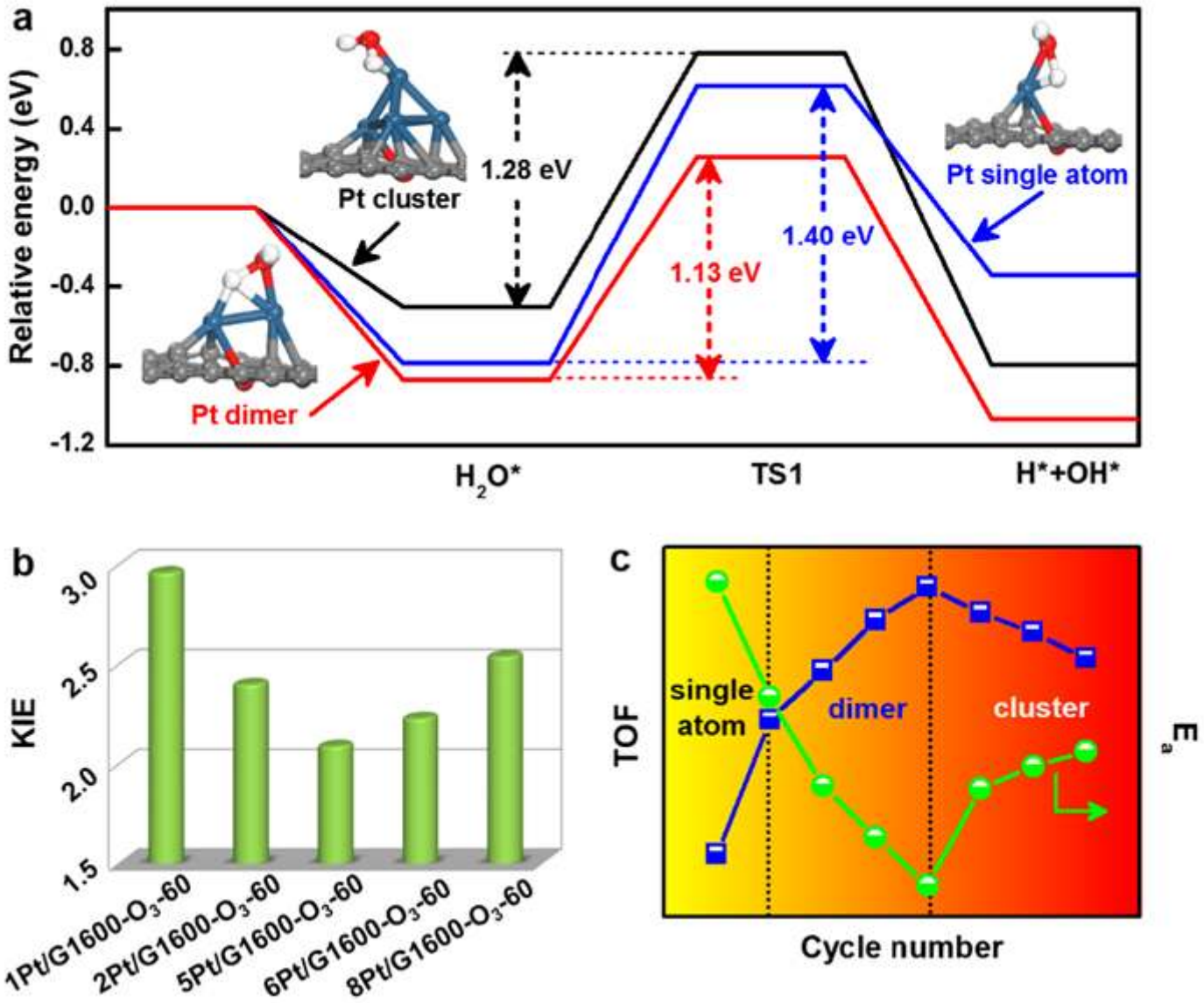

Figure 5

The correlation between size effect of Pt/graphene sub-nanocatalysts and catalytic activity. a, The potential energy diagram of the AB hydrolysis reaction for different Pt catalysts. TS1 is transition state. The ball in gray, blue, red, and white represent carbon, platinum, oxygen, and hydrogen atoms, respectively. b, The kinetic isotope effect (KIE) values of xPt/G1600-O3-60. c, The correlation between the Pt species (single atom, dimer, and cluster) and TOF or activation energy (Ea) for the AB hydrolysis.

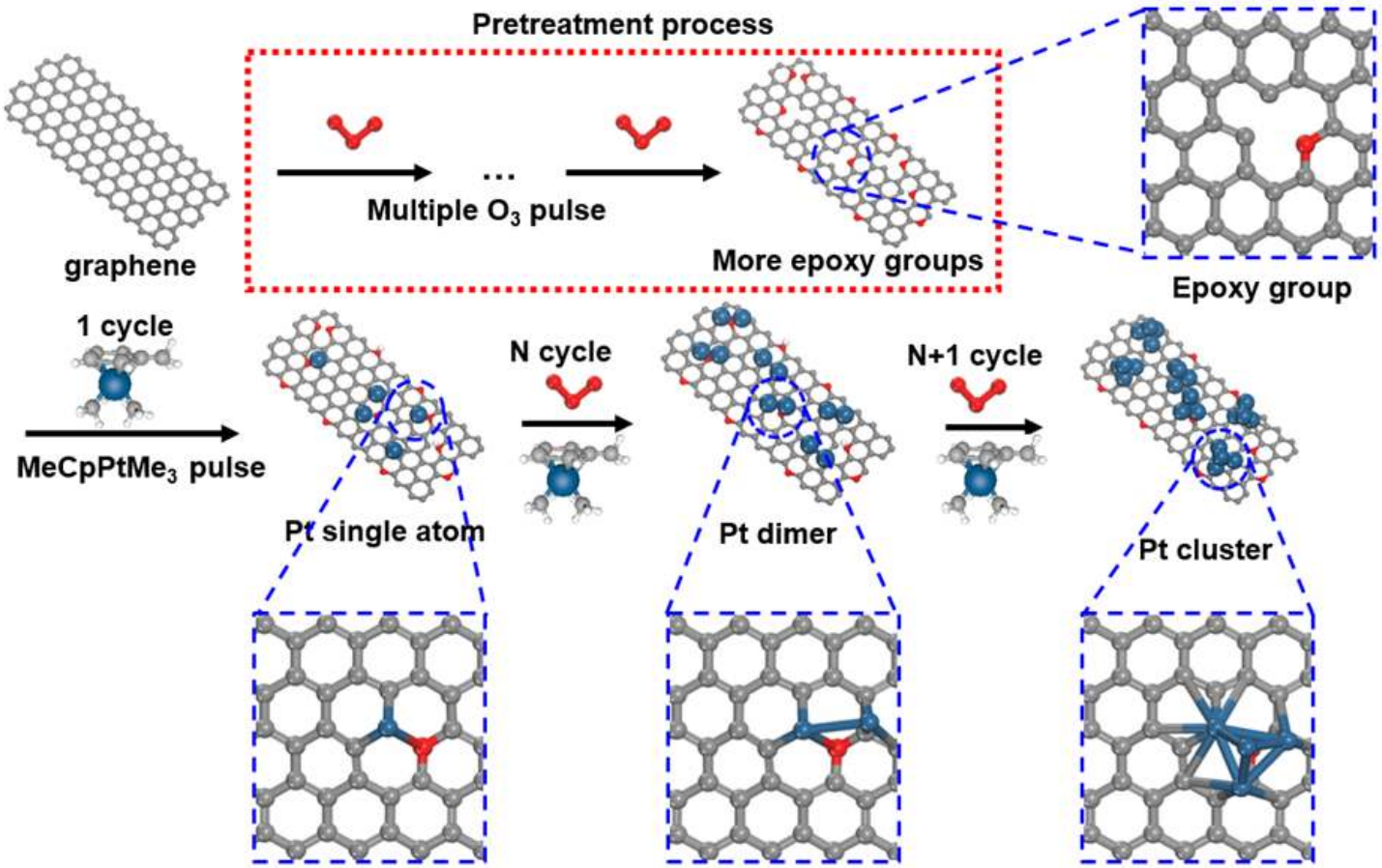

Figure 6

Scheme 1. Design strategy of Pt/epoxy-rich graphene sub-nanocatalysts. Schematic illustration of synthetic processes for precisely controlled Pt single atom, dimer and cluster sub-nanocatalysts supported on graphene with rich in-plane epoxy groups as anchoring sites. The balls in grey, red, white and blue represent carbon, oxygen, hydrogen and platinum.

Supplementary Files

This is a list of supplementary files associated with this preprint. Click to download.

- SupportingInformation.docx